# High-Resolution Structure-from-Motion Models of Hydrothermal Sites in the Central Nevada Seismic Belt: Applications in Hydrothermal, Paleoclimate, and Neotectonic Investigations

Owen A. Callahan, Cassandra A. P. Brigham, Emma Heitmann, Emma Sullivan, Amanda Jackson, Siti R. Mat, Jay Mudambi, Jennifer Osako, Mattathias Needle, Katharine Huntington, and Juliet G. Crider

Department of Earth and Space Sciences, University of Washington, Box 351310, 4000 15th Avenue NE, Seattle, WA 98195-1310 owen.callahan@gmail.com

Keywords: UAV, sinter, travertine, Dixie Valley, Buena Vista Valley

#### **ABSTRACT**

Hot spring travertine and sinter deposits record discharge from hydrothermal systems through evolving hydrothermal, hydrologic, and tectonic regimes. The location and volume of the largest deposits may reflect persistent or particularly robust periods of hydrothermal flow. As part of a broader investigation into the chemical evolution of travertine deposits, we used unoccupied aerial vehicles (UAVs) coupled with high-precision GPS surveys to collect and assemble orthorectified photomosaics and high-resolution digital elevation models (DEMs) using structure-from-motion (SfM) software for eight sites in the northern Central Nevada Seismic Belt. These sites range from large, intrabasin travertine mounds to travertine and sinter deposits offset by Quaternary faults. Some highlights of the research made possible by the acquisition of these topographic datasets include: 1) geomorphic evidence that hydrothermal flow at Hyder Hot Springs has persisted since at least the last highstand of glacial Lake Dixie, 2) documenting the impact of hot spring sinter and hydrothermal alteration on the preservation and morphology of Quaternary fault scarp profiles, 3) mapping the extent of a large extinct travertine deposit in the Stillwater Range, and 4) constraints on the offset of hot spring deposits affected by Quaternary faulting at Kyle Hot Springs. Areas between  $0.51 - 1.23 \text{ km}^2$  (126-303 acres) were easily acquired with less than half a day of surveying and flying, and models capable of producing orthorectified photomosaics and DEMs with average resolution of 2.5 cm/pixel and 9.7 cm/pixel, respectively, were built on a desktop computer with 1-10 days of processing time. In desert landscapes, the resolution of the resulting DEMs approaches that of bare earth LiDAR datasets at a fraction of the cost, with little to no special permitting in most cases, and with limited preplanning. The imagery available and models described herein are freely from the NSF-EAR-funded data facility OpenTopography (https://portal.opentopography.org/datasets) for use in commercial, academic, and educational applications with proper attribution.

#### 1. INTRODUCTION

Geospatial data are fundamental components of geothermal projects across many phases of development, from the relationships between hydrothermal alteration and fault geometry, to pad layout and well trajectory. For broad, surface-based investigations, existing satellite imagery and top ographic data may suffice; however, many inquiries benefit from more data-dense surveys, such as airborne hyperspectral mineral mapping, LiDAR scans, or site-specific engineering schematics. The financial and logistical cost to acquire such data is high and may be beyond the scope of academic investigations or smaller companies in the geothermal sector. For example, terrestrial LiDAR requires transporting heavy, expensive equipment to the field (a complicated task in remote areas), and aerial LiDAR requires the use of an airplane which increases costs of the data acquisition (Pavlis and Mason, 2017).

In recent years, the rapid expansion of unoccupied aerial vehicles (UAV or 'drones') into commercial and recreational markets has been accompanied with a rapid decrease in cost, making aerial imagery available to the masses. With the addition of high-quality cameras, on-board GPS, and third-party structure-from-motion (SfM) software, topographic and outcrop models are much easier to construct on a budget (e.g., Westoby et al., 2012). For example, at the time of this writing, high-end consumer UAVs are an order of magnitude lower in cost than low-end terrestrial LiDAR units, and open-source image-processing software is becoming more accurate and user-friendly (e.g., Froideval et al., 2019, Cutugno et al., 2022).

Like LiDAR, SfM generates point-cloud data sets, but unlike LiDAR, which uses lasers and sensors to collect data, SfM uses photographs. SfM software processes images and automatically solves the geometry of a scene, camera positions, and camera orientations (Westoby et al., 2017). The point clouds are constructed by automatically identifying unique points that appear in many overlapping photos taken from different positions (Lowe, 2004). To align the point cloud to geographic coordinates and reduce potential for distortion in the final model, ground control points (GCPs) are placed throughout the terrain of interest and surveyed with high-precision GPS units. The user subsequently tags the GCPs in the digital photographs to align the point cloud (Westoby et al., 2017).

Data acquired with UAVs can be analyzed in a variety of ways. Digital surface models (DSMs), DEMs, high-resolution orthorectified photomosaics, and polygonal terrain/outcrop models can all be produced from SfM-generated point-clouds. DSMs, DEMs, and photomosaics provide georeferenced 2 and 2.5D data used ubiquitously in GIS software. Polygonal terrain or outcrop models may represent vertical outcrops, overhanging cliffs, or infrastructure that can be explored in 3D space in ways that would not be possible with standard aerial imagery. These models are easily exported into CAD programs and video-game environments to facilitate engineering and design solutions, or to immerse students and stakeholders into a dataset (e.g., Needle et al., 2022). In the geothermal sector specifically, UAVs paired with additional sensors have been used to explore the thermal structure of hydrothermal systems (Harvey et al., 2016; Müller et al., 2022) and even to measure gas emissions above active hydrothermal vents (Zeilinski et al., 2022).

As part of our investigation into the structure and composition of travertine deposits in the northern Central Nevada Seismic Belt, we used UAVs, high-precision GPS surveys, and SfM software to assemble point clouds, 3D models, orthorectified photomosaics, and high-resolution DEMs for eight sites with hydrothermal, paleoclimate, and neotectonic significance (Figure 1). Here we present the model outputs and describe some of the ways in which this dataset is already being utilized in different investigations.

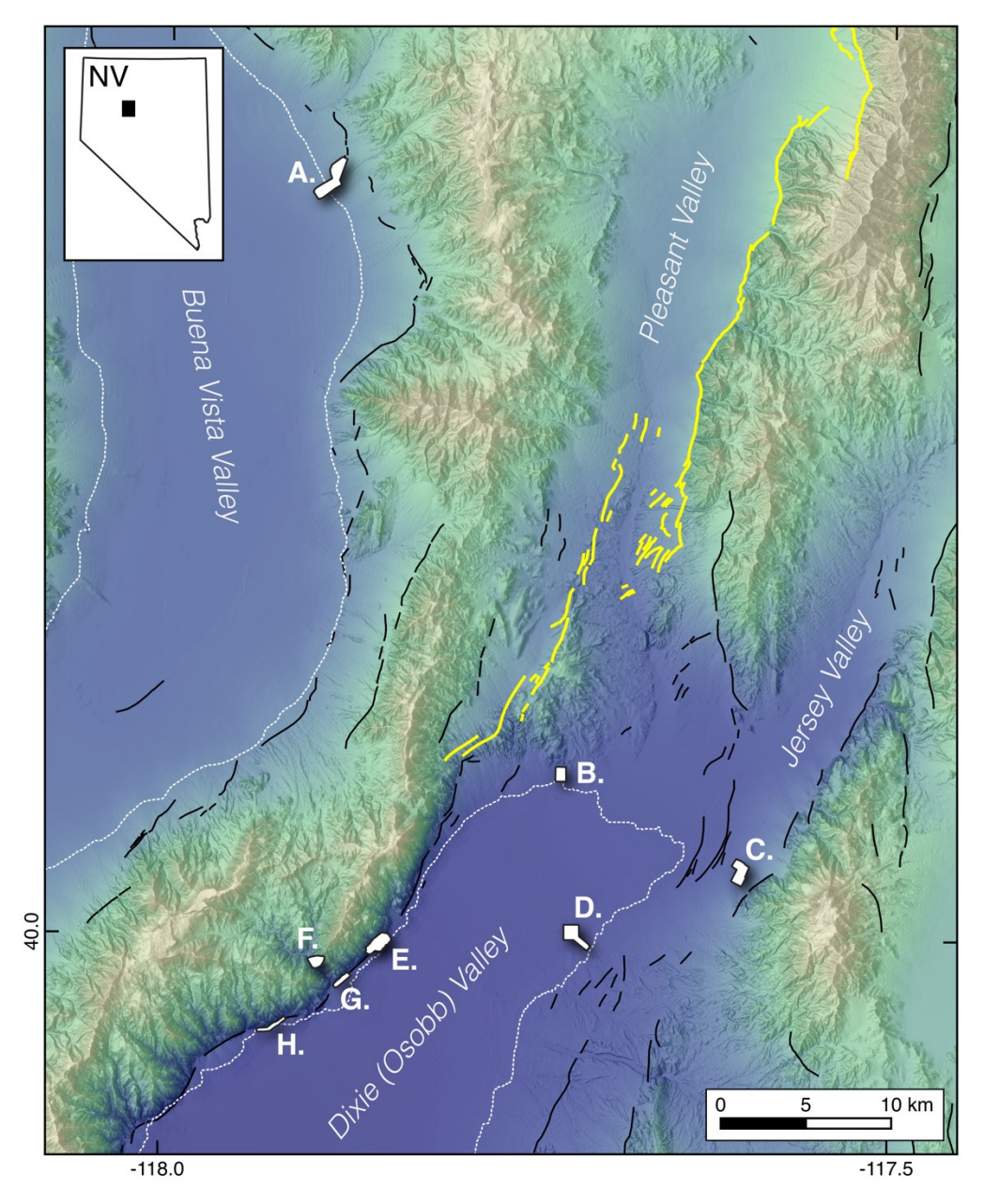


Figure 1. Regional shaded relief map showing the study areas described in the text. From north to south: A. Kyle Hot Springs, sinter mound, and Lake Lahontan shorelines. B. Sou (Seven Devils) Hot Springs. C. Lower Ranch Hot Springs and travertine mound. D. Hyder Hot Springs and Lake Dixie shorelines. E. Senator Fumaroles. F. Cottonwood Canyon "Dead Travertine." G. Travertine and scarp along the Stillwater Range at Cottonwood Canyon. H. Holocene fault scarp, fumaroles, and "Section 10/15" sinter. 1915 Pleasant Valley fault scarps shown in yellow, with older Quaternary faults in black. Late Pleistocene lake highstands (dotted lines) from Reheis (1999).

#### 2. ATTRIBUTES OF THE FIELD AREA

The field area is in an arid part of central Nevada with abundant active faults and older Quaternary fault scarps, relict shorelines from Pleistocene lakes, and surface manifestations of robust hydrothermal systems, all of which leave imprints on the landscape that can be imaged with high-resolution top ographic and photographic surveys. The hydrothermal components of relevance to this conference include producing geothermal fields in Dixie and Jersey valleys, and hot springs, fumaroles, and associated deposits from active and fossil hydrothermal systems across the region. Several active hot springs in Dixie, Jersey, and Buena Vista valleys, including Sou, Hyder, and

Kyle hot springs, are associated with substantial travertine and/or sinter mounds that extend laterally over hundreds of meters and rise several meters above the local topography. Relict deposits formed around extinct hydrothermal systems include large expanses of travertine and sinter as well as exhumed faults, veins, and mineralization. SfM models and some geologic interpretations from eight of these sites are described in the following sections.

The aridity of the sites deserves special mention with respect to the SfM method. Like much of the Basin and Range, the region experiences very low rainfall, from <15 inches per year at higher elevations to around 5 inches per year in the playa (Huntington et al., 2014). Low rainfall contributes to the preservation of geomorphic features, like travertine mounds, fault scarps, and shorelines, that are included in these surveys. The aridity also results in low-lying and sparse vegetation. Although the DEMs derived from these models are technically "surface" models that include the top ographic expression of shrubs and trees, most of the model elevations reflect actual ground surface. In more densely vegetated regions, either specialized filtering techniques (e.g., Anders et al., 2019) or LiDAR are needed to strip away ground cover to produce a bare-earth model.

#### 3. METHODS: AERIAL MAPPING, GPS SURVEYS, AND STRUCTURE-FROM-MOTION MODELS

We prepared ten DEMs and ten orthorectified photomosaics covering  $0.51 - 1.23 \text{ km}^2$  from eight sites in the northern Central Nevada Seismic Belt (Figure 1). These sites include active hot springs associated with travertine and sinter mounds (Kyle, Sou, Lower Ranch, Hyder), regions with active fumaroles (Senator, Frying Pan), and fossil travertine and sinter deposits (Cottonwood, Frying Pan, Kyle, Stillwater Range Front). Surveys at Kyle, Hyder, and Senator were extended laterally to include geomorphic expressions of late Pleistocene shorelines, and Quaternary fault scarps were surveyed at Kyle, Senator, Stillwater Range Front, and Frying Pan fumaroles.

At each site we collected hundreds to thousands of images with a consumer grade DJI Mavic 2 Pro with multiple overlapping flight-paths using vertical and inclined camera angles at  $\leq 100$  m altitude (Figure 2). Flight paths were designed with Pix4Dcapture iOS application, which allows UAV pilots to plan flights with the desired image overlap while factoring in product-specific flight times and return paths. Our sites required a minimum of two to more than five  $\sim 20-30$ -minute flights to cover each area. Especially hot or windy days reduced battery life and resulted in shorter-than-expected flight times, more flights per site, and necessitate multiple backup batteries at some sites.

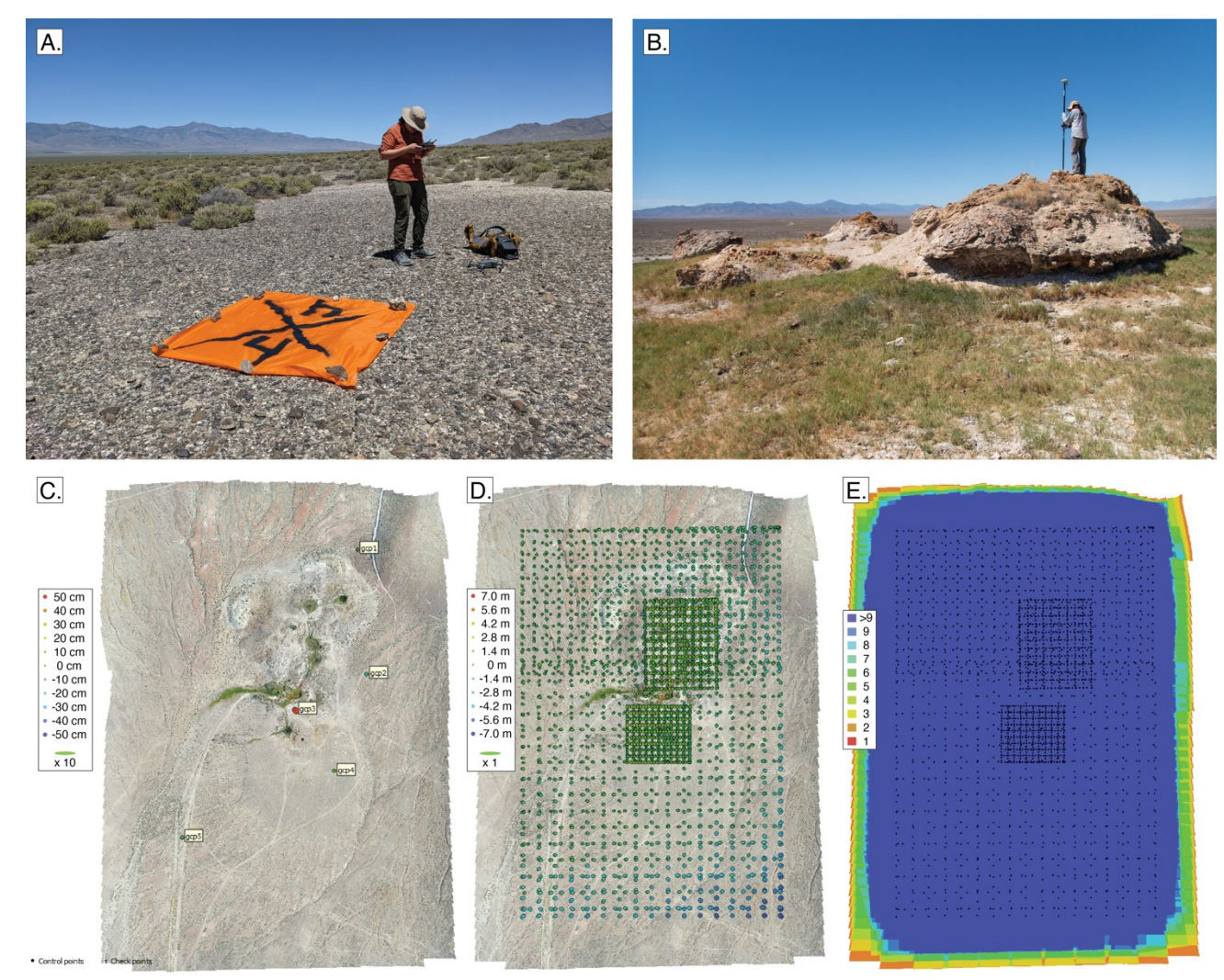


Figure 2 (preceding page). Acquiring and building SfM models. A. Piloting the UAV near Kyle Hot Springs. GCP target in the foreground. B. GPS surveys included GCPs and existing permanent benchmarks where present, such as the one being surveyed here at Hyder Hot Springs. Metadata reports from the SfM software include: GCPs and associated vertical (color) and horizontal (diameter) error (C), camera locations and associated error (D), and the number of images used in each cell to build the point cloud (E).

We used Trimble R2 GNSS receivers to collect GPS locations at 2-5 GCPs and any existing permanent benchmarks in the survey areas (Figure 2). Each GCP was marked with a 4 m², high-visibility numbered target deployed for the duration of the UAV survey. During model construction, GCPs were manually identified in the photographs and assigned their known, surveyed locations.

SfM models were built using Agisoft Photoscan Professional version 1.4.5 on an Intel Core i7-4790 CPU @ 3.60GHz with 32.0 GB of RAM. Processing and build time from import to export ranged from less than one day for the smaller areas and lowest resolution models to more than 10 days for larger, higher resolution models. Build time is highly sensitive to computer processing speed, software version, and desired resolution. Cloud-based processing is also available (e.g., Nocerino et al., 2017) and would reduce the demand on personal workstations.

The orthorectified photomosaics and DEMs derived from the SfM models offer substantial improvement over existing imagery and topographic data (Figure 3).

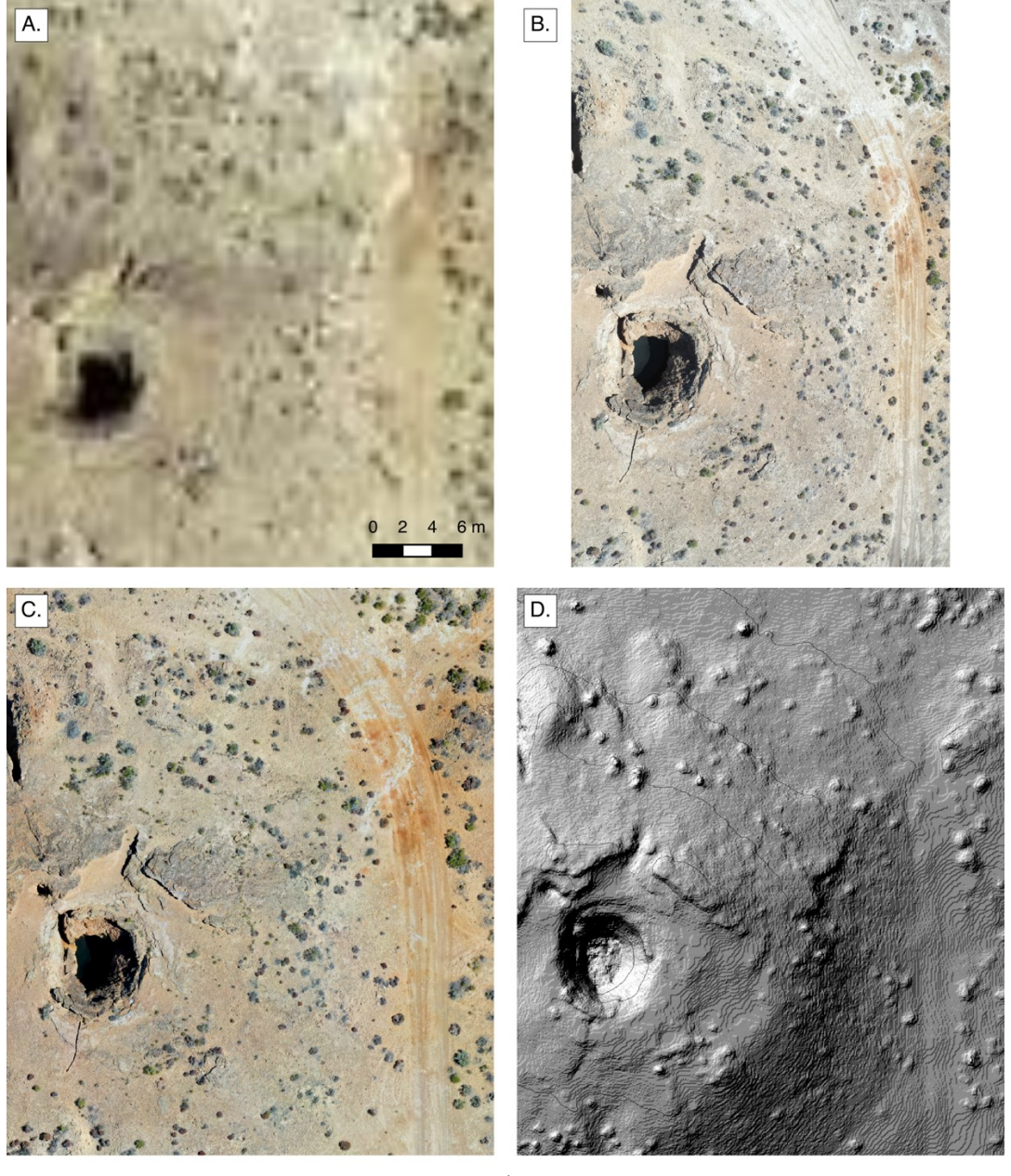


Figure 3 (preceding page). Comparing UAV images and model products with Google satellite imagery at Sou Hot Springs. A. Existing Google satellite imagery showing a portion of the main cone. B. A single low altitude (~30 m) image acquired with UAV. The narrower width is due to camera inclination. C. Orthorectified photomosaic derived from UAV images and SfM model. D. Shaded relief derived from DEM with 1 meter contour interval. Note scrub brush and track ruts resolved in shaded relief.

## 4. STRUCTURE-FROM-MOTION MODELS AND APPLICATIONS

In the following subsections we highlight the quality of the data and demonstrated applications of the site-specific SfM-based orthoimagery and high-resolution DEMs acquired in this study. In total, ten models were built at eight sites from the Dixie and Buena Vista valley portions of the Central Nevada Seismic Belt. From north to south, these sites are Kyle Hot Springs, Sou Hot Springs, Lower Ranch Hot Springs, Hyder Hot Springs, Senator Fumaroles, Cottonwood Canyon Travertine, Stillwater Range Front in the Seismic Gap Section of the Dixie Valley Fault, and Frying Pan Fumaroles and the Section 10/15 sinter. Some highlights of the research enabled by these models include: improved fault maps at Kyle Hot Springs, geomorphic evidence that hydrothermal flow at Hyder Hot Springs has persisted since at least the Late Pleistocene, mapping the extent of a large extinct travertine deposit in the Stillwater Range, and measuring the impact of hot spring sinter and hydrothermal alteration on the morphology of Quaternary fault scarps. Full resolution images and DEMs of the following models are freely available from the NSF-EAR-funded data facility Open Topography at <a href="https://doi.org/10.5069/G9P26WBB">https://doi.org/10.5069/G9P26WBB</a> (Callahan et al., 2023).

## 4.1 Kyle Hot Springs

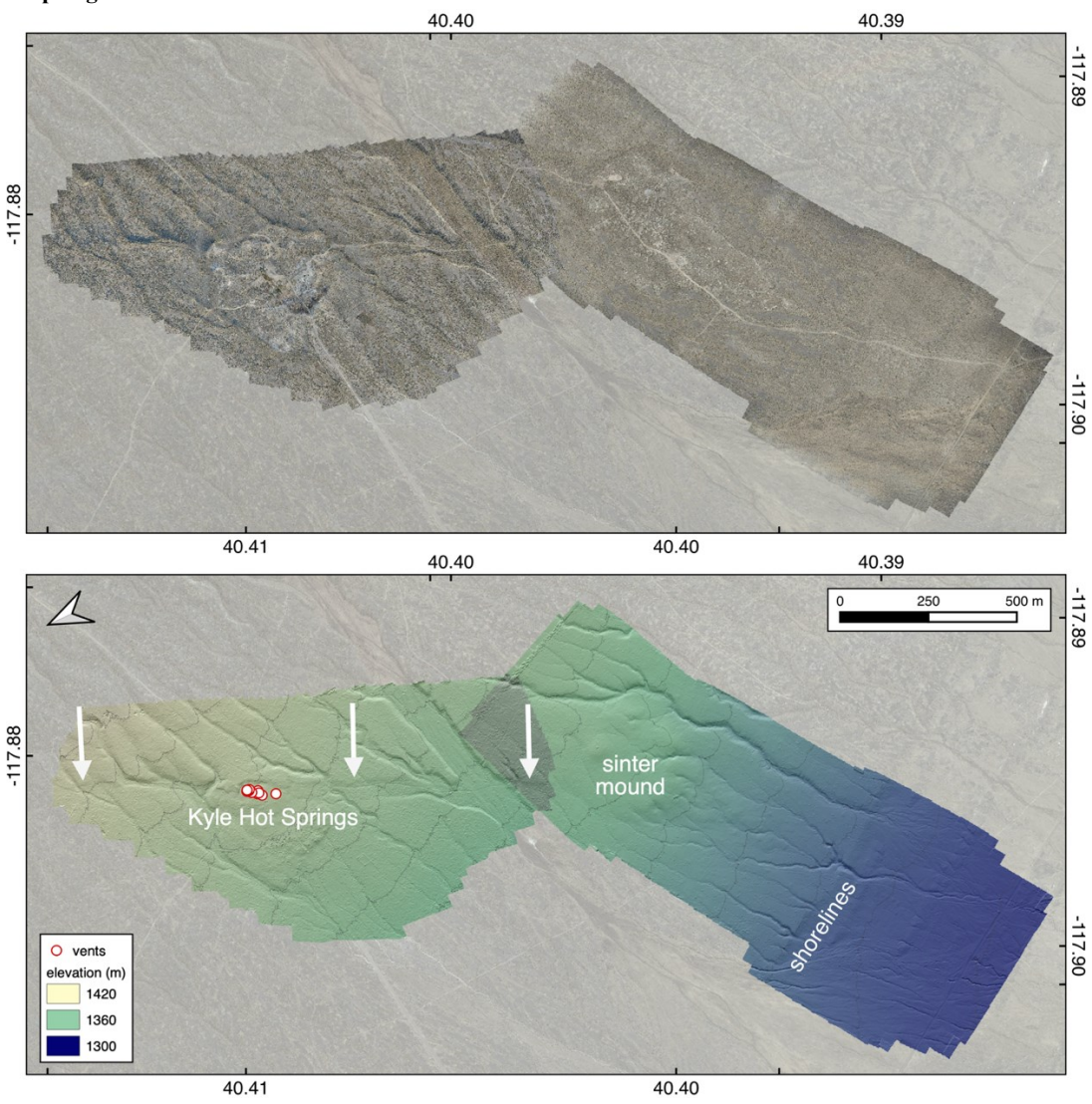


Figure 4. Orthorectified photomosaics (top) and structure-from-motion DEMs (bottom) of the Kyle Hot S prings area, Buena Vista Valley. The northern travertine and sinter mound (to the left in this view) contains active hot springs that vent through a fractured carapace. The southern sinter mound is extinct. White arrows show the top edge of the Quaternary Buena Vista Valley scarp. Lake Lahontan shorelines truncate the alluvial fan to the southwest.

Kyle Hot Springs in Buena Vista Valley is a stunning example of fault-controlled hydrothermal discharge (Site A in Figure 1). Two mounds are included in the surveys from this location, an older, inactive sinter mound to the south and a presently active travertine and sinter mound to the north. The high-resolution DEM shows that the northern mound is cut by a scarp of undetermined age associated with the Buena Vista Valley fault system (Figure 4).

We built two adjacent DEMs and orthorectified photomosaics of the region around Kyle Hot Springs. The first region was collected on June 13, 2021, and extends ~1650 m NE-SW, from a relict sinter mound south of Kyle Hot Springs at the southern terminus of the Buena Vista Valley fault to the Late Pleistocene shores of Lake Lahontan. The DEM and orthorectified photomosaic were derived from an SfM model built with 1874 vertical and inclined images, 5 GCP markers, 210 thousand tie points, and a 92-million-point dense cloud. The wireframe model contains 6 million faces and the resulting resolution of the photomosaic and DEM are 2.8 cm/pixel and 11.0 cm/pixel, respectively. The calculated vertical error in GCPs in the Agisoft model ranges from -2 cm to +10 cm. The second area was collected on March 26, 2022, and covers a region approximately 1420 m SSW-NNE by 730 m ESE-WNW around the active hot spring mound and along the Buena Vista Valley Fault scarp. This model was built from 2444 aligned images, 5 GCP markers, 412 thousand tie points, and a 201-million-point dense cloud. The model has 40 million faces and the resulting orthorectified photomosaic and DEM resolution is 2.0 cm/pixel and 7.9 cm/pixel, respectively. The calculated vertical error in GCPs in the Agisoft model is -0.7 m to +3.5 m. The hot spring is on private property, and this survey was collected with permission of the owner.

## 4.2 Sou Hot Springs

Sou Hot Springs is located in northern Dixie Valley at the foot of the Sou Hills (Site B in Figure 1). This dataset was collected as a base for mapping hydrothermal features, including active hydrothermal discharge, relict travertine mounds, and local topography and geomorphology. This deposit differs from Kyle Hot Springs in that it lacks clear surface expression of local fault control; there are subtle breaks in slope that may be related to tectonic deformation, but these are small and could be related to travertine deposition and fluvial erosion. However, the site does contain fissures that post-date photographic surveys from the 1800s and intra-mound unconformities in the travertine, the timing of which are currently under investigation.

The DEM and orthorectified photomosaic at Sou Hot Springs in northern Dixie Valley cover an area encompassing approximately 850 m N-S by 600 m E-W around the springs, mounds, and foothills (Figure 5). The model was constructed from 2599 aligned images collected on June 15, 2021, five GPS-surveyed GCP markers, and 436 thousand tie points. A 104-million-point dense cloud was used to build a 3D model with 21 million faces, and a 7.7 cm/pixel DEM. The orthorectified photomosaic resolution is 1.9 cm/pixel. Calculated error in GCPs in the Agisoft model ranges from -20 cm to +50 cm. Sou Hot Springs is on private property, and the survey was flown with permission of the owner.

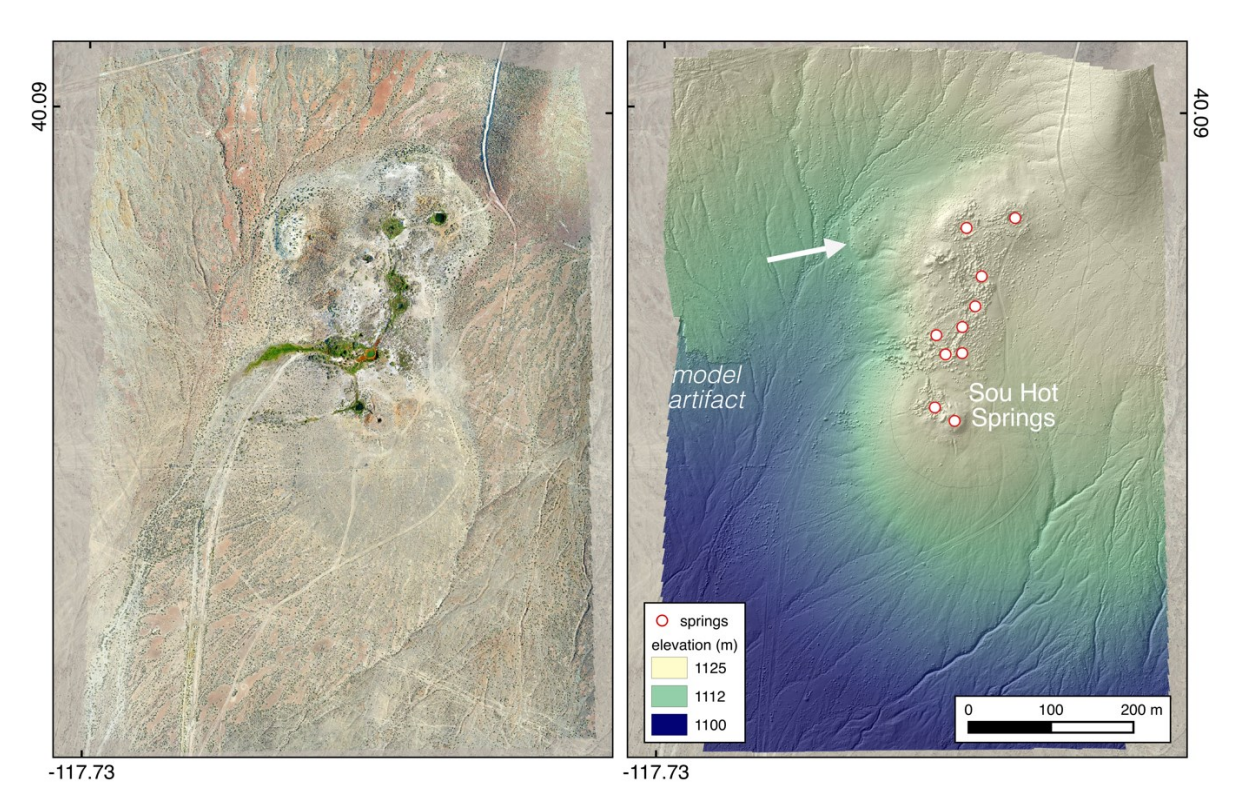


Figure 5. Orthorectified photomosaic (left) and structure-from motion DEM (right) of the Sou (Seven Devils) Hot Springs area showing hot and warm springs, pools, and flowing wells. SfM artifacts show as topographic roughness in areas with poor image coverage or quality. A subtle scarp of unknown origin occurs north of the main mound.

#### 4.3 Lower Ranch Hot Springs and Travertine Mound

The Lower Ranch springs and travertine mound are located in the northwestern part of Dixie Valley near the base of Cain Mount ain (Site C in Figure 1). The travertine deposit is one of the largest deposits in the region and likely formed in the Late Pleistocene (Goff et al., 2002). Small, warm springs are currently located at the top and at the base of the travertine mound, but most of the mound is inactive. Little else has been reported about this deposit, however the new DEM and orthorectified photomosaic provide a useful basemap for future investigations. Features of note that are discernible in the imagery and topographic model include a steep scarp in the NW portion of the deposit that seems to truncate the deposit, but which is also overlapped by travertine deposits with waterfall morphology, and subtle pool-and-terrace slope morphology in the northern part of the deposit (Figure 6).

We collected 2629 vertical and inclined images and surveyed five GCPs at Lower Ranch Hot Springs and travertine mound on June 18, 2021. These images were coordinated with 176 thousand tie points, leading to an 86-million-point dense cloud and a 3D model with 17 million faces. The resulting DEM has a resolution of 12.3 cm/pixel and the orthorectified photomosaic has a resolution of 3.1 cm/pixel. Calculated error in GCPs in the Agisoft model ranges from +9 cm to +45 cm. The survey covered the area encompassing the travertine mound and modern low-flow thermal springs, approximately 1290 m ~SW-NE by 950 m NW-SE. The western part of the survey and access to the mound is on or through private property and was flown with permission of the owner. Private dwellings were removed from the final products.

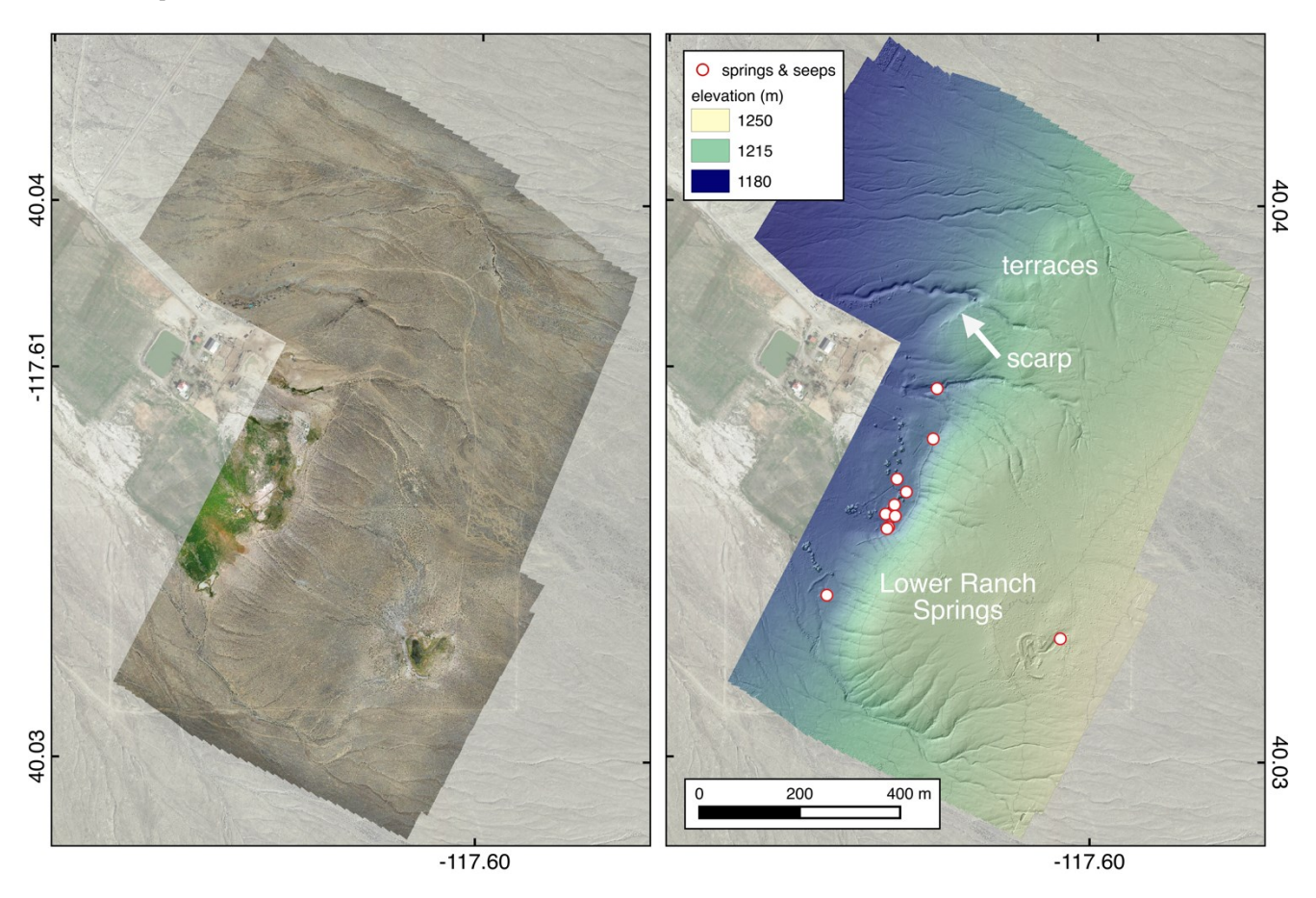


Figure 6. Orthorectified photomosaic (left) and structure-from-motion DEM (right) of Lower Ranch hot springs and travertine mound. SfM model reveal a potential faulted-related scarp, terrace morphology in the north, and moderately dissected deposits in the main travertine area.

## 4.4 Hyder Hot Springs

Hyder Hot Springs is an active, intrabasin, travertine mound measuring 250 m in diameter and rising 18 m above the local topography in northern Dixie Valley (Site D in Figure 1). The mound contains 9 active travertine cones or fans with discharge temperatures up to ~80 °C. The site was originally surveyed to facilitate mapping of surface hydrothermal features. However, during field investigations we noted distinct geomorphic expressions of the old travertine mounds that appeared to coincide with Lake Dixie highstand elevations. This was later confirmed with GPS surveys of GCPs at benchmarks and shorelines during the flights. Details revealed in these surveys supports the hypothesis that Hyder Hot Springs has persisted as a hydrothermal feature since at least the Late Pleistocene Lake Dixie highstand (Callahan et al., 2021, and work in progress).

We constructed two datasets from surveys at Hyder Hot Springs to help resolve the relationship between the mound elevations and the highstand shoreline (Figure 7). The first survey was flown on June 14, 2021, and covers the region extending approximately 900 m E-W by 900 m N-S around the active hot springs mound. The second region was flown on June 15, 2021, and extends ~1560 m from the modern mound in the northwest to gravel beach bars surveyed by Caskey and Ramelli (2004) in the southeast. The first model was built from 2672 aligned images. The model contains 306 thousand tie points, a 95-million-point dense cloud, and 6 million faces. The resolution of the resulting orthorectified photomosaic is 1 cm/pixel, with a 9.9 cm/pixel DEM built from the dense cloud. The calculated error in GCPs in the Agisoft model ranges from +12 cm to -15 cm. The second model was built from 1608 aligned images, 171 thousand tie points, a 368-million-point dense cloud, and 74 million faces. The resolution of the resulting orthorectified photomosaic is 2.1 cm/pixel, and the DEM resolution is 4.2 cm/pixel. The calculated error in GCPs in Agisoft model ranges from +24 cm to -40 cm. Both models include five GPS-surveyed GCPs and a NOAA benchmark at the top of the mound.

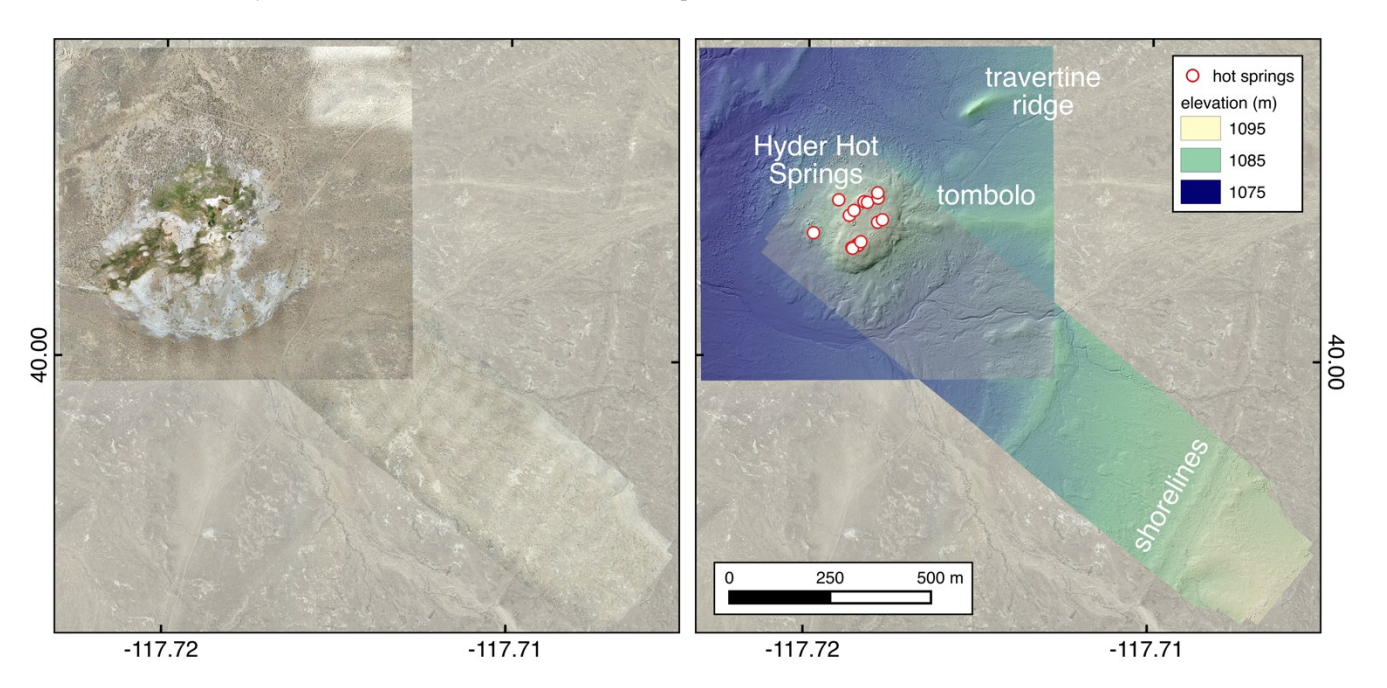


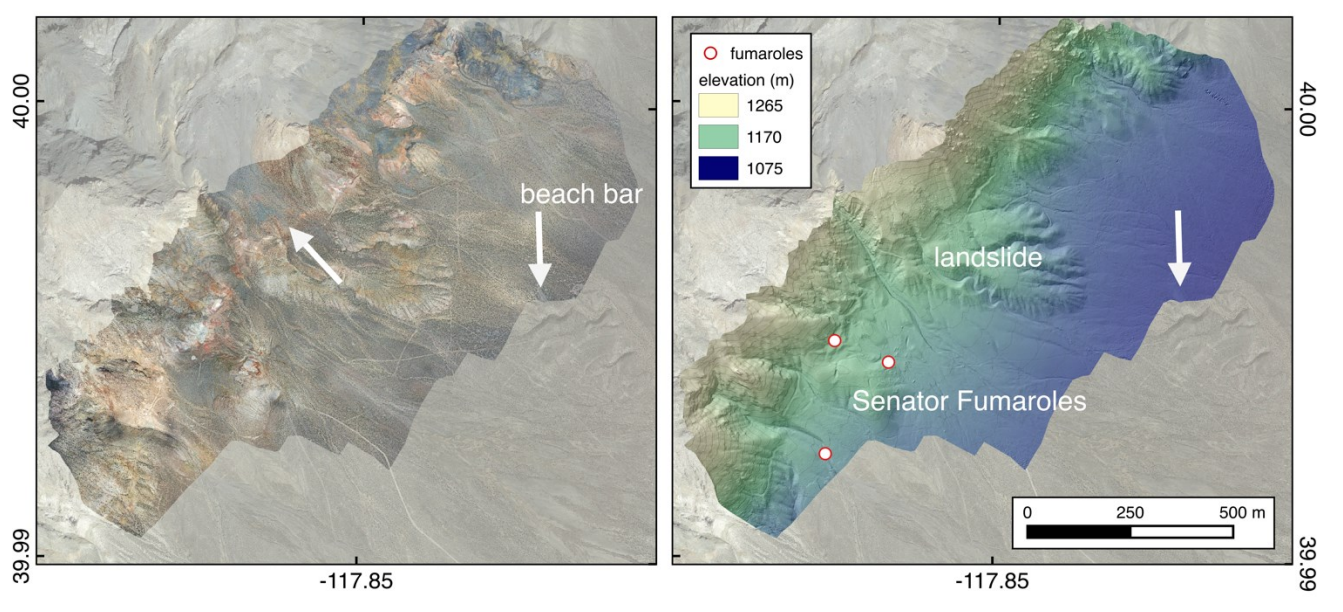
Figure 7. Orthorectified photomosaic (left) and structure-from-motion DEM (right) of the Hyder Hot S prings region. Active hot and warm springs were mapped using high-resolution orthoimagery basemaps. The elevation of the mound with respect to Lake Dixie shorelines in the southwest part of the DEM, and a potential tombolo east of the main mound, support the hypothesis that the mound was a topographic feature during the Late Pleistocene highstand of the lake.

#### 4.5 Senator Fumaroles

Senator Fumaroles is located at the base of the Stillwater Range in northern Dixie Valley (Site E in Figure 1). The area includes active fumaroles and distributed acid sulfate alteration, as well as cryptic range-front scarps, dissected mass-wasting deposits, and a Lake Dixie highstand (Figure 8). The DEM and imagery provide a useful basemap for describing the occurrence of the fumaroles, which are distributed between the range front and upper fan (Figure 8). The DEM and GCP surveys also show the top of the beach bar is several meters lower than other Lake Dixie highstand shorelines to the east and further south in the Stillwater Range (Caskey and Ramelli (2004). This provides a useful datum for Holocene normal fault displacement at the range front, which appears to truncate large mass wasting deposits sourced to the west.

The DEM and orthorectified photomosaic at Senator Fumaroles were built from images collected on March 29, 2022, of the area extending 1540 m along the range front. The model was constructed from 1078 aligned images with 223 thousand tie points and a 43-million-point dense cloud, and includes 9 million faces. Three of five surveyed GCP markers are included in the model. The orthorectified photomosaic resolution is 3.1 cm/pixel and the DEM resolution 12.5 cm/pixel. The calculated error in GCPs in the Agisoft model is -2.4 m to +0.6 m. Unfortunately, the resolution and quality of the orthomosaic at Senator Fumaroles is lower than the other areas due in part to an overly ambitious pilot and a particularly steep range front. If any one finds a drone west of the main fumarole field, please contact the authors.

Figure 8 (proceeding page). Orthorectified photomosaic (left) and structure-from-motion DEM (right) of the Senator Fumaroles area. Active fumaroles, warm ground, and acid sulfate alteration occur at the range front and cutting basin-ward landslide deposits at the top of the alluvial fan. A lower elevation lake highstand bar to the east, and a subtle range-front scarp to the west, are consistent with Holocene normal fault displacement in this portion of the Stillwater Seismic Gap (Wallace and Whitney, 1984).



#### 4.6 Cottonwood Canyon Travertine

The Cottonwood Travertine, also known as the Dead Travertine in Goff et al. (2002) and Lutz et al. (2002), is a large, sloping fan deposit covering a steep canyon wall 1.5-2 km west of the Stillwater Range front (Site F in Figure 1). Jackson et al. (this volume) present the first outcrop map of the Cottonwood Canyon travertine deposit using the DEM and orthorectified photomosaics from our survey as basemaps for their investigation. They describe the deposit extending from calcite-cemented gravels ~150 m above the canyon floor, with subtle mounds and onlapping travertine in several locations down the face of the apron. The thickest preserved portion of the deposit may be as much as 13 m thick, with the northwestern portion of the canyon wall only covered by a few meters or less of layered travertine (Jackson et al, this volume).

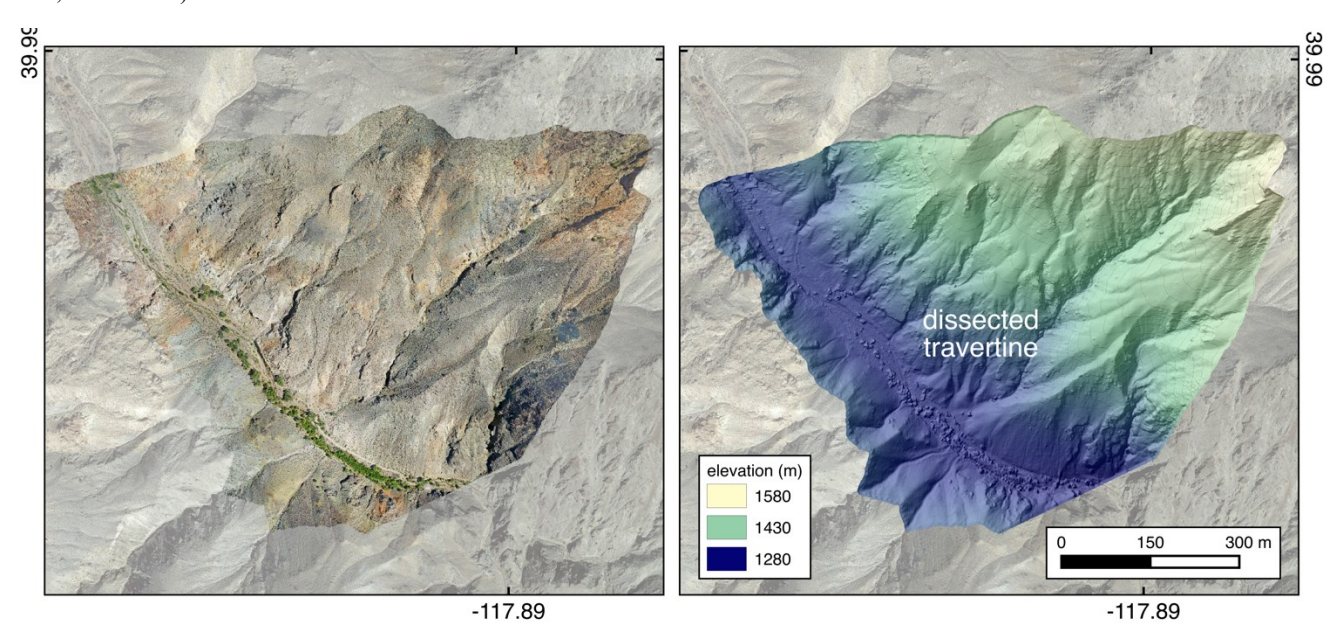


Figure 9. Orthorectified photomosaic (left) and structure-from-motion DEM (right) of the Cottonwood Canyon travertine. The orthorectified basemap was used for mapping the distribution of dissected travertine deposits described in Jackson et al. (this volume).

The SfM model of the Cottonwood Canyon deposit was built from 1681 aligned images acquired on June 16, 2021. The mapped region extends approximately 900 m ~NE-SW by 750 m NW-SE (Figure 9). The model was built with 463 thousand tie points and two GCPs surveyed with GPS, and includes a 36-million-point dense cloud and 7 million faces. The orthorectified photomosaic resolution is 3.9 cm/pixel and the resolution of the DEM is 15.6 cm/pixel. The reported error in GCPs in the Agisoft model are sub-centimeter due to the limits of two-point fitting. Two factors impacted the resolution and accuracy of this model. First, the region is rugged, with local relief over 300 m and limited line of sight. The steep top ography blocks images from some locations, requiring a greater density of overlapping

flights with a wider variety of camera angles to adequately cover the region. Furthermore, most of the area was flown above the intravalley ridges at 1540 m elevation, resulting in less resolution on the valley floor. Second, after the 2+ km hike into the site we learned a valuable lesson about confirming that all five GCPs are in fact packed with the survey gear, thus limiting our ability to fully ground-truth the locations.

#### 4.7 Northern Stillwater Seismic Gap

The base of the Stillwater Range north of Cottonwood Canyon and west of the producing Dixie Valley geothermal field (Site G in Figure 1) contains scarps possibly related to Holocene displacement within the Stillwater Seismic Gap (Wallace and Whitney, 1984), veins and cemented talus exposed by the scarp, an exhumed profile of the fault zone architecture, and small outcrops of travertine. The features in this region are more cryptic than in the other models containing active hydrothermal manifestations, younger faults, and shorelines. The DEM and mosaic were acquired to improve mapping outcomes of the scattered travertine and carbonate veins that occur in the damage zone of this portion of the fault, which manifests as a break in slope and brighter talus in the DEM and imagery (Figure 10).

The structure-from-motion model covers approximately 1,130 m of the Stillwater Range Front north of Cottonwood Canyon and includes 413 aligned images containing five GCPs acquired on March 25, 2022. The model was built from 243 thousand tie points and a 46-million-point dense cloud and has 9 million faces. The DEM resolution is 10.2 cm/pixel and the orthorectified photomosaic resolution is 2.6 cm/pixel. The GCPs in this model were included as known tie points but were not surveyed with GPS. The calculated error in GCPs in the Agisoft model ranges from -70 cm to +56 cm. This was one of the fastest datasets to acquire and build: the area only required two orthogonal flights and the GCP were deployed but not surveyed.

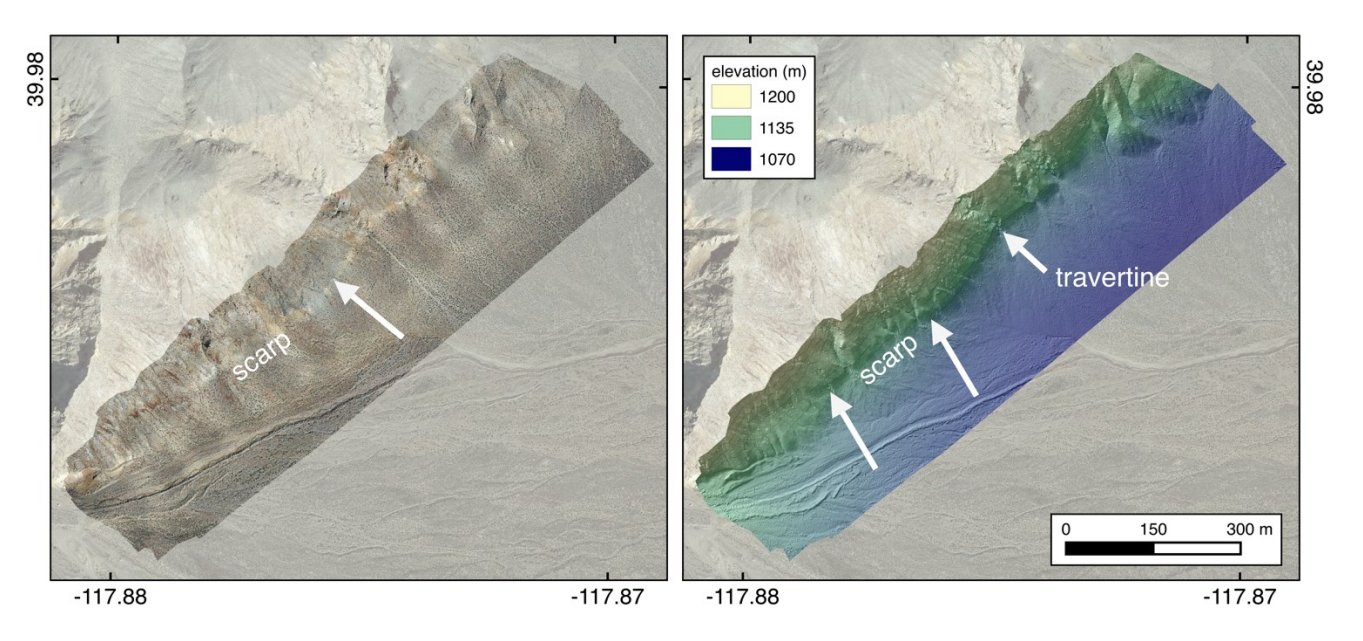


Figure 10. Orthorectified photomosaic (left) and structure-from-motion DEM (right) of a portion of the northern Stillwater Seismic Gap near the mouth of Cottonwood Canyon. A possible Quaternary fault scarp shows up as a lighter band of rock and talus in the orthoimage and a distinct break in slope in the DEM. Travertine and dilatational calcite-lined veins are abundant in the fault zone. The fault cross-section is exposed in a wall of the quarry at the southern end of the model.

### 4.8 Frying Pan Fumaroles

The Fry ing Pan Fumaroles and Section 10/15 sinter deposits described by Lutz et al. (2002) are located at the base of the Stillwater Range southwest of the producing geothermal field (Site H in Figure 1). The location includes weak active fumaroles, Holocene sinter mounds (gey serite) and cemented gravel, and a fault scarp in the Stillwater Seismic Gap section of the Dixie Valley fault zone that postdates the sinter. Brigham and Callahan (2022) used the high-resolution DEM from this site to compute the morphologic variability of scarp-normal top ographic profiles (Brigham and Crider, 2022) in uncemented gravels, sinter and sinter-cemented gravels, and in the region affected by fumarole alteration. They found differences in scarp height and scarp morphometrics depending on the composition of the substrate. In uncemented gravels scarp profiles have a mean height of  $6.2~(\pm 0.9)$  m and exhibit low morphologic variability, with rounded convex-upward crests and concave-upward toes. The section of the scarp that cuts sinter and cemented gravels has a mean height of  $5.8~(\pm 0.8)$  m and a more variable profile, ranging from broad concave-upward slopes to multi-tiered free faces and notches. In the fumarole-altered material, the individual Holocene rupture is difficult to discern, possibly due to modification by ongoing hydrothermal activity.

The Frying Pan Fumaroles model covers an area stretching approximately 1840 m along the Stillwater Range front containing the active fumaroles, extinct sinter deposits, and fault scarps from the Holocene 'Gap Event' that was flown and surveyed on June 16, 2021 (Figure 11). The model contains 2429 aligned images and five GPS-surveyed GCPs, 844 thousand tie points, a 169-million-point dense cloud, and 11 million faces. The resulting orthorectified photomosaic resolution is 1.5 cm/pixel and the DEM resolution is 6.0 cm/pixel. Calculated Z error in GCPs in Agisoft model ranges from +1.5 m to -0.6 m.

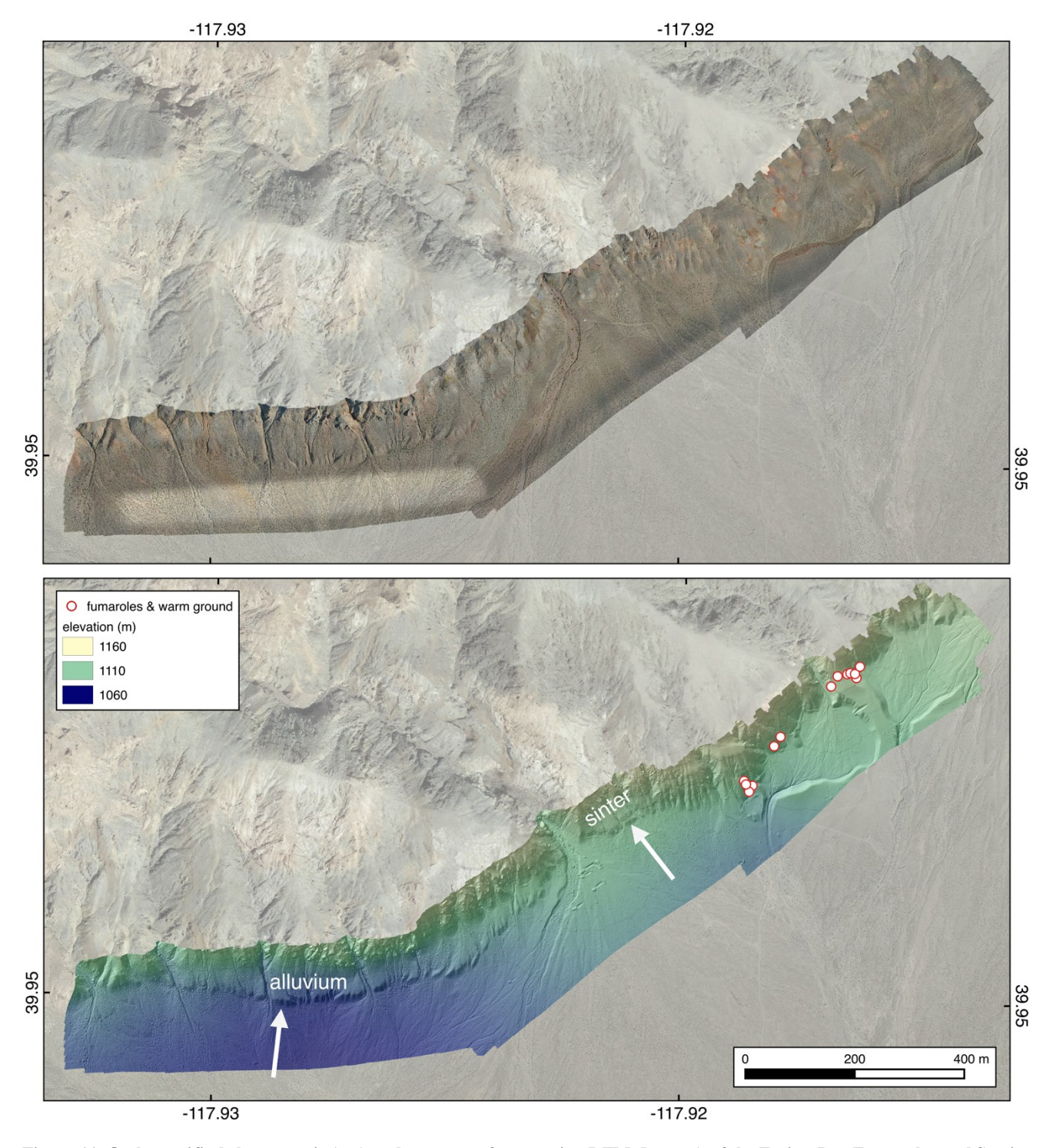


Figure 11. Orthorectified photomosaic (top) and structure-from motion DEM (bottom) of the Frying Pan Fumaroles and Section 10/15 sinter. Orthorectified images were used as a basemap during field investigations of active fumaroles and warm ground. The high-resolution DEM improved descriptions of fault scarp morphology discussed in Brigham and Callahan (2022). The bright patch in the lower left is due to different image exposures and may be related to changing cloud conditions.

## 5. CONCLUSION

Advances in UAV technology have made low elevation aerial photography accessible to a wide market. With additional third-party commercial and open-source software utilizing structure-from-motion techniques, these images can be combined to create 3D models,

high-resolution digital surface models, and orthorectified photomosaics. In sparsely vegetated regions of the western US, the resulting datasets approach the quality of bare earth models generated with LiDAR at a fraction of the cost. These products have uses in a variety of geothermal applications, from mapping for geoscience investigations to topside engineering problems. We presented ten DEMS and orthorectified photomosaics from eight sites in Dixie and Buena Vista valleys, Nevada. These sites contain active hot springs and fumaroles, travertine and sinter deposits, and a variety of other geomorphic features from the Central Nevada Seismic Belt that have not been presented in high-resolution datasets before. These products are available and free to use with attribution from Open Topography (https://doi.org/10.5069/G9P26WBB). Please let us know if you are interested in using these models for research or commercial projects.

## **ACKNOWLEDGMENTS**

This work was supported by NSF EAR Tectonics Award #2040716 to OAC, JGC, and KH, and a grant from the Quaternary Research Center to OAC and JGC. Funds from the NSF GeoALLIES program (Award #2037292) supported undergraduate fieldwork in 2022. We also wish to thank the landowners for permission to access private land included in these surveys.

#### REFERENCES

- Anders, N., Valente, J., Masselink, R., and Keesstra, S.: Comparing Filtering Techniques for Removing Vegetation from UAV-Based Photogrammetric Point Clouds, Drones, 3(3), (2019), 61. <a href="https://doi.org/10.3390/drones3030061">https://doi.org/10.3390/drones3030061</a>
- Brigham, C. A. P., and Callahan, O. A.: Hot Spring Sinter, Acid Sulfate Alteration, and Morphologic Variation in Fault Scarp Profiles from the Stillwater Seismic Gap, Dixie Valley, NV, Annual Geothermal Rising Conference, Reno, NV (2022).
- Brigham, C. A. P., and Crider, J., G.: A New Metric for Morphologic Variability Using Landform Shape Classification via Supervised Machine Learning, Geomorphology, 399, (2022). https://doi.org/10.1016/j.geomorph.2021.108065
- Callahan, O. A., Brigham, C. A. P., Heitmann, E., Sullivan, E., Huntington, K., Loewy, S., and Crider, J. G.: Geomorphic Evidence for Long-Lived Hydrothermal Circulation at Hyder Hot Springs, Nevada, GSA Annual Meeting, Portland, OR (2021).
- Callahan, O. A., et al.: DEMs and Orthomosaics of Hydrothermal Sites in the Central NV Seismic Belt. Hosted by Open Topography, (2023), https://doi.org/10.5069/G9P26WBB
- Caskey, S. J., and Ramelli, A. R.: Tectonic Displacement and Far-Field Isostatic Flexure of Pluvial Lake Shorelines, Dixie Valley, Nevada, Journal of Geodynamics, 38(2), (2004), 131-145. https://doi.org/10.1016/j.jog.2004.06.001
- Cutugno M, Robustelli U, and Pugliano G.: Structure-from-Motion 3D Reconstruction of the Historical Overpass Ponte della Cerra: A Comparison Between MicMac® Open-Source Software and Metashape®, Drones, 6(9), (2022), 242. https://doi.org/10.3390/drones6090242
- Froideval, L., Pedoja, K., Garestier, F., Moulon, P., Conessa, C., Pellerin Le Bas, X., Traoré, K., and Benoit, L.: A Low-Cost Open-Source Workflow to Generate Georeferenced 3D SfM Photogrammetric Models of Rocky Outcrops, The Photogrammetric Record, 34, (2019), 365-384. https://doi.org/10.1111/phor.12297
- Goff, F., Bergfeld, D., Janik, C. J., Counce, D., and Murrel, M.: Geochemical Data on Waters, Gases, Scales, and Rocks from the Dixie Valley Region, Nevada (1996-1999), LA-13972-MS, (2002). <a href="https://www.osti.gov/servlets/purl/894412">https://www.osti.gov/servlets/purl/894412</a>
- Harvey, M. C., Rowland, J. V., and Luketina, K. M.: Drone with Thermal Infrared Camera Provides High Resolution Georeferenced Imagery of the Waikite Geothermal Area, New Zealand, Journal of Volcanology and Geothermal Research, 325, (2016), 61-69. https://doi.org/10.1016/j.jvolgeores.2016.06.014
- Huntington, J. M., Garcia, C. A., and Rosen, M. R.: Hydrogeologic Framework and Occurrence, Movement, and Chemical Characterization of Groundwater in Dixie Valley, West-Central Nevada, Scientific Investigations Report 2014-5152, USGS, (2014). https://doi.org/10.3133/sir20145152
- Jackson, A., Callahan, O. A., Heitmann, E., Schauer, A., Brigham, C. A. P., Mat, S. R., Mudambi, J., Osako, J., Huntington, K., and Crider, J. G.: Paleothermometry of an Enigmatic Travertine Deposit: Cottonwood Travertine, Stillwater Range, NV, Proceedings, 48<sup>th</sup> Workshop on Geothermal Reservoir Engineering, Stanford University, Stanford, CA, (2023).
- Lowe, D.: Distinctive Image Features from Scale-Invariant Keypoints. International Journal of Computer Visualization, 60, (2004), 91-110. https://doi.org/10.1023/B:VISI.0000029664.99615.94
- Lutz, S. J., Caskey, S. J., Mildenhall, D. D., Browne, P. R. L., and Johnson, S. D.: Dating Sinter Deposits in Northern Dixie Valley, Nevada - The Paleoseismic Record and Implications for the Dixie Valley Geothermal System, Proceedings, 27<sup>th</sup> Workshop on Geothermal Reservoir Engineering, Stanford University, Stanford, CA, (2002).
- Müller, D., Walter, T. R., Zimmer, M., and Gonzalez, G.: Distribution, Structural and Hydrological Control of the Hot Springs and Geysers of El Tatio, Chile, Revealed by Optical and Thermal Infrared Drone Surveying, Journal of Volcanology and Geothermal Research, 432, (2022). https://doi.org/10.1016/j.jvolgeores.2022.107696
- Needle, M. D., Mooc, J., Akers, J. F., and Crider, J. G.; Virtual Field Experiences in a Web-Based Video Game Environment: Open-Ended Examples of Existing and Fictional Field Sites, Geoscience Communication, 5(3), (2022), 251-260. https://doi.org/10.5194/gc-5-251-2022

- Nocerino, E., Poiesi, F., Locher, A., Tefera, Y. T., Remondino, F., Chippendale, P., and Van Gool, L.: 3D Reconstruction with a Collaborative Approach Based on Smartphones and a Cloud-Based Server, International Archives of the Photogrammetry, Remote Sensing and Spatial Information Sciences, 42(W8), (2017), 187-194. https://doi.org/10.5194/isprs-archives-XLII-2-W8-187-2017
- Pavlis, T. L., and Mason, K. A.: The New World of 3D Geologic Mapping, GSA Today, 271(10), (2017), 4-10. https://doi.org/10.1130/GSATG313A.1
- Reheis, M. C. (Cartographer): Extent of Pleistocene Lakes in the Western Great Basin, Miscellaneous Field Studies Map 2323, USGS, (1999). https://doi.org/10.3133/mf2323
- Wallace, R. E., and Whitney, R. A.: Late Quaternary History of the Stillwater Seismic Gap, Nevada. Bulletin of the Seismological Society of America, 74(1), (1984), 301-314.
- Westoby, M. J., Brasington, J., Glasser, N. F., Hambrey, M. J., and Reynolds, J. M.: 'Structure-from-Motion' Photogrammetry: A Low-Cost, Effective Tool for Geoscience Applications, Geomorphology, 179, (2012), 300–314. <a href="https://doi.org/10.1016/j.geomorph.2012.08.021">https://doi.org/10.1016/j.geomorph.2012.08.021</a>
- Zielinski, L. A., Glen, J. M., Earney, T. E., Rea-Downing, G. H., Vaughan, R. G., Kelly, P. J., Keller, G. H., Dean, B. J., and Schermerhorn,
  W. D.: UAS-Based Tools for Mapping and Monitoring Hydrothermal Systems: An Example from Mammoth Lakes, California,
  Geothermal Resources Council Transactions, 46, (2022), 1618-1637.